Biosensors and Bioelectronics 226 (2023) 115132

Contents lists available at ScienceDirect

Biosensors and Bioelectronics

journal homepage: www.elsevier.com/locate/bios

Dual-quenching electrochemiluminescence resonance energy transfer system from CoPd nanoparticles enhanced porous g-C_3N_4 to FeMOFs-sCuO for neuron-specific enolase immunosensing

Lihua Hu [a,*], Tengfei Shi [a], Jiye Chen [a], Qianqian Cui [a], Hao Yu [a], Dan Wu [a], Hongmin Ma [a], Qin Wei [a], Huangxian Ju [a,b]

[a] Collaborative Innovation Center for Green Chemical Manufacturing and Accurate Detection, Key Laboratory of Interfacial Reaction & Sensing Analysis in Universities of Shandong, School of Chemistry and Chemical Engineering, University of Jinan, Jinan, 250022, PR China
[b] State Key Laboratory of Analytical Chemistry for Life Science, School of Chemistry and Chemical Engineering, Nanjing University, Nanjing, 210023, PR China

ARTICLE INFO

Keywords:
Electrochemiluminescence
P–C_3N_4-CoPdNPs
FeMOFs-sCuO
Dual-quenching
NSE detection

ABSTRACT

For the diagnosis and therapy of small cell lung cancer (SCLC), the accurate and sensitive determination of neuron-specific enolase (NSE) content is crucial. This work outlines a dual-quenching electrochemiluminescence resonance energy transfer (ECL-RET) immunosensor based on the double quenching effects of iron base metal organic frameworks (FeMOFs) loaded with small sized CuO nanoparticles (FeMOFs-sCuO) towards CoPd nanoparticles (CoPdNPs) enhanced porous g-C_3N_4 (P–C_3N_4-CoPdNPs). To be specific, we prepared a porous g-C_3N_4 (P–C_3N_4) which has a rich porous structure, and significantly increased the specific surface area and the number of reaction sites of P–C_3N_4. Meanwhile, the CoPdNPs were loaded onto P–C_3N_4 to improve the ECL luminescence property of P–C_3N_4/$K_2S_2O_8$ system through acting as a coreaction accelerator. In addition, the ultraviolet–visible (UV–vis) absorption spectra of FeMOFs and small sized CuO nanoparticles (sCuO) showed considerable overlap with the ECL emission spectra of P–C_3N_4 appropriately. Therefore, FeMOFs with high specific surface area were prepared and well combined with sCuO to effectively dual-quenching the ECL emission of P–C_3N_4 based on resonance energy transfer. Hence, a new type ECL-RET couple made up of P–C_3N_4-CoPdNPs (donor) and FeMOFs-sCuO (acceptor) were developed for the first time. A certain amount of P–C_3N_4-CoPdNPs, Ab_1, BSA, NSE were modified layer by layer onto the electrode surface. Then FeMOFs-sCuO-Ab_2 bioconjugates was incubated through the immune recognition binding. As a result, a sandwich-type ECL biosensor was manufactured successfully for NSE immunoassay. Under optimal experimental conditions, the limit of detection (LOD) and the limit of quantitation (LOQ) of the prepared ECL sensor for NSE analysis was 20.4 fg mL^{-1} and 7.99 fg mL^{-1}, respectively, with the relative standard deviation (RSD) of 1.68%. The linear detection range was 0.0000500–100 ng mL^{-1}. The studied immunosensor had satisfactory sensitivity, specificity and reproducibility, manifesting the suggested sensing strategy might offer a good technical means and theoretical basis for the sensitivity analysis of NSE and has a potential application in clinical diagnosis analysis.

1. Introduction

One of the deadliest types of cancer, lung cancer, claims many lives each year all over the world. Small cell lung cancer (SCLC) and non-small cell lung cancer (NSCLC) are two categories for it. Due to SCLC's initial great sensitivity to chemotherapy, but also because of its propensity for early metastasis and rapid doubling time, as well as its frequent relapses and developed chemoresistance, the disease is challenging to treat (Xu et al., 2015). Neuron-specific enolase (NSE) has been shown in studies to be a trustworthy, accurate, and sensitive blood marker for diagnosing SCLC in its early stages (Maet al., 2020). Human serum typically contains NSE at levels between 5 and 12 ng mL^{-1}, therefore their elevated levels are a sign that SCLC development is highly likely (Amani et al., 2018). NSE was used to monitor the recurrence of small cell lung cancer 4–12 weeks earlier than clinically confirmed recurrence. In order to track the development and effectiveness of therapeutic therapy for SCLC in clinical diagnosis, it is crucial to determine NSE levels.

* Corresponding author.
E-mail address: hulihua1206@163.com (L. Hu).

https://doi.org/10.1016/j.bios.2023.115132
Received 9 August 2022; Received in revised form 2 February 2023; Accepted 5 February 2023
Available online 6 February 2023

The process known as electrochemiluminescence (ECL) involves species produced at electrodes going through electron transport processes to generate excited states that emit light (Tang et al., 2022). In the meantime, a redox reaction between the reactants contained the light emission process (Zhang et al., 2019). ECL immunoassay has attracted extensive attention in the area of modern biosensors due to the low signal background, broad linear range and prominent sensitivity, and simple operation (Cao et al., 2020; X.J. Li et al., 2020; Majdoub et al., 2020). The exceptional ECL feature of the luminous reagent forms the foundation of a superior ECL sensing technique. Graphite phase carbon nitride (g-C_3N_4), with layered structure, good biocompatibility, chemical stability, good electrochemical properties and other characteristics (Wang et al., 2020; Y. Wang et al., 2019; Z. Wang et al., 2019), have been widely used in catalysis (Song et al., 2018), fluorescence (Rahbar et al., 2018), electrochemistry (Liu et al., 2020) and other areas. However, the performance of g-C_3N_4 has an important relationship with its specific surface area and pore structure. In addition, the composition of carrier also affects the wide application of g-C_3N_4 to a large extent. Therefore, porous g-C_3N_4 (P–C_3N_4) was prepared herein by template etching of small sized silicon dioxide (SiO_2), which gave it a rich porous structure, greatly increased specific surface area, optimized the reaction site and charge separation. In addition, CoPd nanoparticles (CoPdNPs) were found to significantly strengthen the ECL luminescence property of P–C_3N_4/$K_2S_2O_8$ system, who can be defined as a coreaction accelerator. Thus, the excellent electrochemical luminescence performance of CoPdNPs enhanced porous g-C_3N_4 (P–C_3N_4-CoPdNPs) was first discovered.

Energy transmission technology at the nanoscale realized the electrochemiluminescence resonance energy transfer (ECL-RET) method. Additionally, this technology requests that the receptor's UV–Vis absorption spectrum and the donor's ECL spectrum overlaps. Metal-organic frameworks (MOFs), have found use in a variety of fields including sensing (Feng et al., 2019; Pan et al., 2019), catalysis (Sun et al., 2018), gas storage and separation (Daglar et al., 2021). In recent years, MOFs have become a research hotspot because of the high surface area, variable pore morphology, diverse structure and good electrochemical stability (Hu et al., 2019; Ye et al., 2019). Iron base MOFs (FeMOFs) with easy synthesis, controllable particle size, good solubility in water (Zhao et al., 2022) and broad UV–vis absorption spectra (Fu et al., 2017), has been considered as a good recipient in ECL-RET system. In addition, the existence of abundant carboxyl and amino ensures that the biofunctionalization of FeMOFs as probe is easy to implement (Zou et al., 2018). So the FeMOFs can be used as labels in various analysis strategy (Luan et al., 2018; Zhao et al., 2016; Zhang et al., 2020). Copper oxide (CuO) nanoparticles have many advantages, such as good chemical stability, large surface area, suitable band edge position and extended light absorption range (Dalkiran and Brett, 2022; Din et al., 2022; Xuan et al., 2021). It is a good photosensitive material and are widely used in optical, electrical, semiconductor and electrode materials. In the present work, the UV–Vis absorption spectra of small sized CuO nanoparticles (sCuO) were found to overlap with the ECL emission spectra of P–C_3N_4 well. In addition, the easy-prepared FeMOFs with large specific surface area were applied to load sCuO to obtain FeMOFs-sCuO nanocomposites as a dual-quenching probe. Moreover, the UV–vis absorption peak of sCuO becomes more obvious after combination with FeMOFs, which can better overlap with the emission spectrum of P–C_3N_4, further improved the RET interaction between P–C_3N_4-CoPdNPs and FeMOFs-sCuO. So FeMOFs-sCuO can be expected to effectively extinguish the luminescence of P–C_3N_4.

Herein, the excellent electrochemical luminescence performance of P–C_3N_4-CoPdNPs was found and studied for the first time. In addition, the easy-prepared FeMOFs with large specific surface area were applied to load sCuO to obtain FeMOFs-sCuO nanocomposites, which can be used as a quenching probe for P–C_3N_4-CoPdNPs. Based on the RET interaction from P–C_3N_4-CoPdNPs to FeMOFs-sCuO, a quehch-type electrochemical luminescence biosensor was firstly manufactured for sensitive analysis of NSE. This work can provide a new theoretical basis and method reference for the clinical analysis of many more biomolecules.

2. Experimental section

2.1. Preparation of P–C_3N_4-CoPdNPs

P–C_3N_4 was synthesized based on the report (Erbaycu et al., 2010) and the supplementary material provided explicit instructions. CoPdNPs was synthesized according to known methods (Wang et al., 2016). In 18 mL of oleylamine, cobalt acetylacetonate (0.35 mmol) and palladium bromide (0.30 mmol) were dissolved. The mixture was then reacted in nitrogen atmosphere at 60 °C while being stirred. The mixture appeared pink during the reaction. Following the addition of trioctylphosphine (0.5 mL), the color of the reaction system changed to dark green. With a heating rate of 5 °C min^{-1}, the mixture was heated to 260 °C, then held there for 2 h. The solution was then chilled until it reached room temperature. The CoPdNPs could be produced by centrifuging after adding ethanol (40 mL). The produced CoPdNPs underwent two hexane (20 mL) and ethanol (30 mL) washes. The resulting solid were then redispersed in hexane.

P–C_3N_4 (250 mg) were dissolved in ethanol (20 mL). The prepared CoPdNPs dispersion solution (8 mL) was centrifuged and dispersed in anhydrous ethanol (20 mL), after ultrasonic, it was mixed with p-C_3N_4 solution and stirred overnight. The solution was treated by centrifugation with a rate of 7000 r min^{-1}, washed multiple times with ethanol, then redispersed in ethanol.

2.2. Preparation of FeMOFs

FeMOFs was prepared as the method described previously (Zhang et al., 2020). 2-aminoterephthatic acid (0.126 g), $FeCl_3{\cdot}6H_2O$ (0.187 g), and acetic acid (3.0 μL) were dissolved in N,N-dimethylformamide (15 mL). The solution was subsequently reacted for 4 h at 120 °C. Next, the reaction mixture was treated by centrifugation and washed by N, N-dimethylformamide three times and ethanol once. At last, the collected solid was vacuum-dried at 60 °C.

2.3. Preparation of FeMOFs-sCuO-Ab_2

sCuO were prepared as the method described previously (Chen et al., 2012). and the supplementary material provided explicit instructions. sCuO nanoparticles (40 mg) and FeMOFs (20 mg) were dispersed in ethanol (150 mL), ultrasonic dispersion followed by stirring overnight. Then the product was centrifuged, washed with anhydrous ethanol three times, then vacuum-dried overnight at 55 °C.

100 μL Ab_2 (10 μg mL^{-1}), 200 μL EDC (10 mmol) and NHS (5 mmol) mixture PBS (pH 7.4) solution and 1 mL PBS (pH 7.4) were incubated at 4 °C for 4 h. Next, 1.5 mg FeMOFs-sCuO were added and incubated at 4 °C for 12 h, then the mixture was centrifuged and dissolved in 1 mL PBS and then stored at 4 °C for further use.

2.4. Fabrication of the biosensor

The preparation procedure of the biosensor is relatively simple (Scheme 1). Glassy carbon electrode (GCE, $\Phi = 4$ mm) was given a 0.05 μm alumina slurry pretreatment to achieve a clean and clear surface. On the GCE's surface, 6 μL P–C_3N_4-CoPdNPs were constructed and allowed to air dry. Then, 6 μL $Ab_1$was attached, allowed by BSA (3 μL, 0.1 wt%) to take up the nonspecific adsorption sites. Thereafter, a series of different concentrations of NSE (6 μL) were spread onto the modified electrode, and stored for 4 h at 4 °C in a moist state. Finally, the ECL biosensor was manufactured after the immune recognition binding of 6 μL FeMOFs-sCuO-Ab_2 bioconjugates, followed by storing at 4 °C for later use. In the above construction process, the as-prepared electrode was

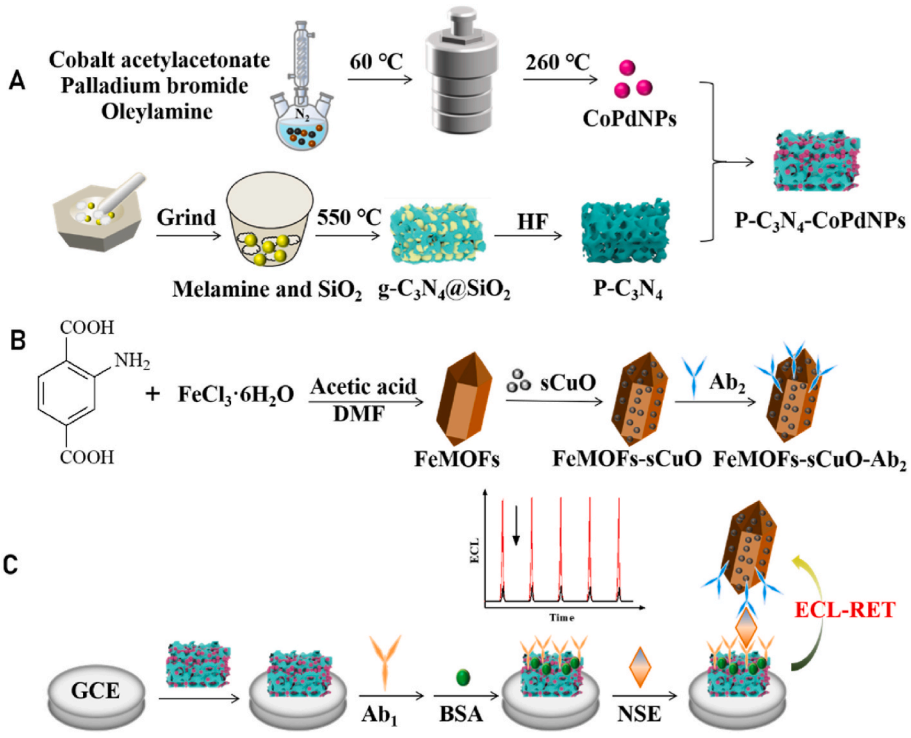

Scheme 1. Synthetic procedure of the composite materials and layer upon layer modification procedure of the NSE immunosensor.

softly rinsed with PBS buffer solution after each modification step to remove weakly-bound components.

2.5. ECL measurements

The classical three-electrode system was applied to investigate the ECL signal, in which Ag/AgCl as reference electrode, platinum electrode as counter electrode, and the electrode with different modification states as working electrode. Cyclic voltammetry (CV) was used to measure the electrochemical response between −1.5 and 0 V at a scanning rate of 0.15 V s^{-1}. To achieve the best results and identify the ECL responses to NSE with a range of various concentrations, the measurement was performed in ECL cell contained PBS (10 mL, pH 7.4) with $K_2S_2O_8$ (80 mM). The voltage of photomultiplier tube was 680 V. Subsequently, the fabricated immunosensor was put in the cell and investigated the ECL performance. A digital photograph of the ECL experimental setup was shown in Fig. S1.

2.6. The procedure of analysis of NSE in serum samples

In order to conduct the recovery experiment, the human serum was obtained from a local hospital and diluted 10 times before use. First, the NSE concentration of the diluted serum was measured by using immunosensor fabricated here (denoted as detected concentration). Then the samples were divided into four groups, and each group was spiked with 0.0500, 0.100, 0.500, 1.00 ng mL^{-1} of NSE standard samples, respectively (denoted as addition). After measurement, the corresponding NSE concentrations of these samples were obtained.

3. Results and discussion

3.1. Material characterization

The morphologies and structure characterization of the synthesized materials were researched by electron microscopy technologies. As shown in the scanning electron microscopy (SEM) of Fig. 1A, SiO_2 nanospheres with uniform size of about 15 nm were obtained. As shown in Fig. 1B, and SiO_2 nanospheres were tightly wrapped by g-C_3N_4, presenting a bulk structure as a whole of g-C_3N_4@SiO_2. After the removal of SiO_2 by 10% HF etching, the internal and surface of fluffy g-C_3N_4 were filled with pores with a size of 15–20 nm, which greatly increases the specific surface area of P–C_3N_4 (Fig. 1C). The prepared CoPdNPs were equably dispersed with a uniform particle size of about 10 nm (Fig. 1D). Transmission electron microscopy (TEM) image of the P–C_3N_4 was shown in Fig. 1E, which clearly shows a multilayer superposed bulk structure with abundant pore. The size of CoPdNPs was smaller than the holes size of the P–C_3N_4, so that CoPdNPs could be well loaded on both the interior and surface of the P–C_3N_4, and the TEM image confirmed that the uniform load was successfully achieved (Fig. 1F). FeMOFs with a length of about 2 μm and a diameter of about 600 nm were successfully prepared, presenting a perfect bicuspid hexagonal columnar crystal with very uniform size and morphology (Fig. 1G). SEM image and TEM image of sCuO displayed in the supplementary information (Fig. S2) revealed that the product consisted of spherical particles with a regular morphology and a diameter of 10 nm. As shown in Fig. 1H, the surface of FeMOFs was occupied by many sCuO particles, verifying a high and stable load of sCuO onto FeMOFs (Fig. 1H). In addition, SEM image and its corresponding EDS elemental maps (Fig. 1I) were utilized to present P–C_3N_4-CoPdNPs preparing not only its morphology but also the existence of Co and Pd elements.

X-ray diffraction (XRD) was further applied to indicate the internal molecular structure of composite materials. The obvious diffraction peaks at 26.50° and 46.19°corresponds to the planes of (002) and (201) of P–C_3N_4 (Fig. 2A, curve a). When the CoPdNPs was combined, new peaks appeared in the overall diffraction pattern, which were at 33.98°, 38.55°, 40.53°, 43.64° and 51.54° corresponding to the planes of (004), (301), (114), (220), (401) of Co elements, respectively. In addition, the peak values of 40.01°, 46.53° and 67.92° also appeared in the diffraction pattern, corresponding to the planes of (111), (200) and (220) of Pd element, which confirmed the successful preparation of the P–C_3N_4-CoPdNPs composite material (Fig. 2A, curve b). As shown in Fig. 2B, the XRD pattern of FeMOFs were consistent with those reported in the

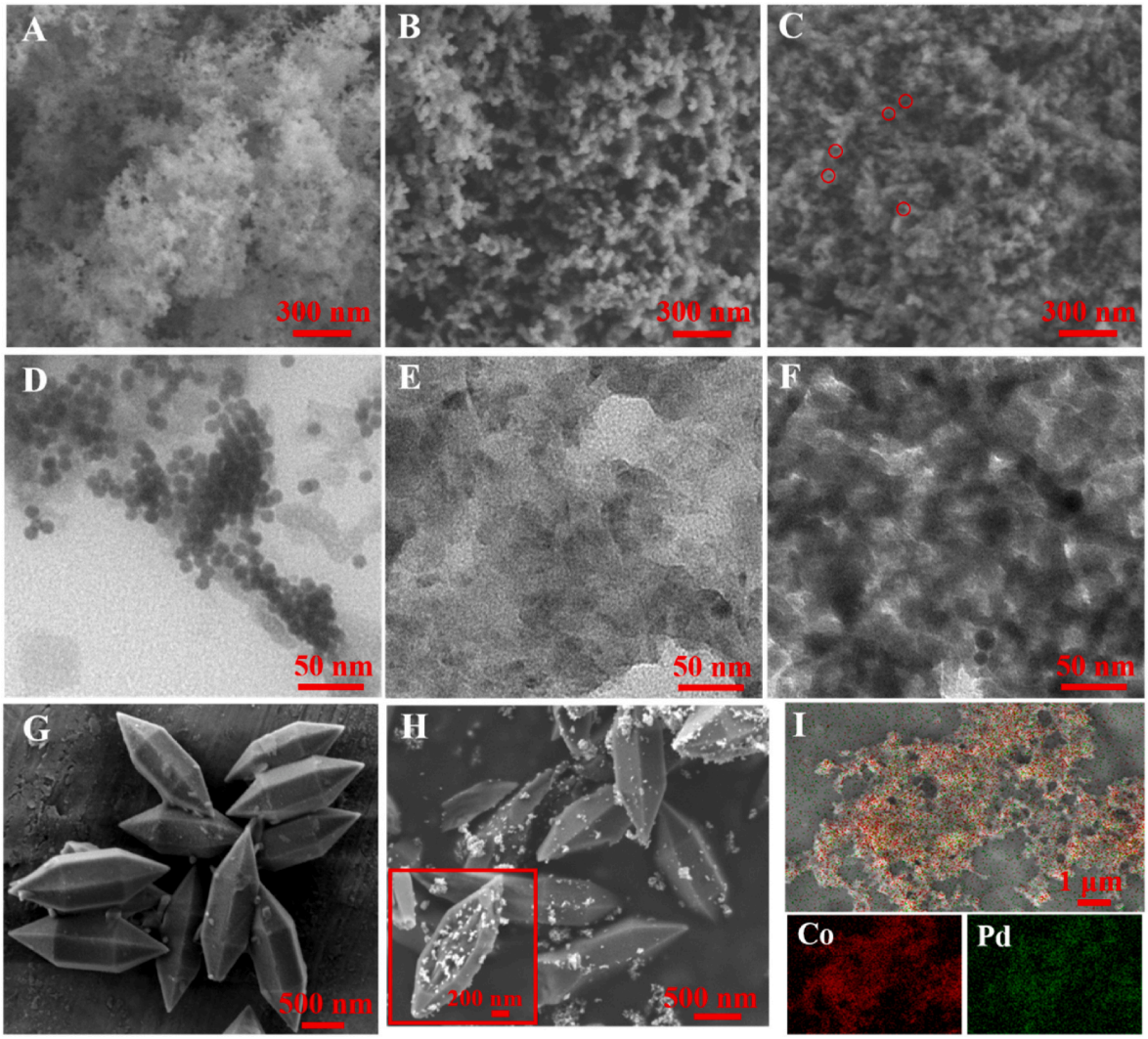

Fig. 1. SEM images of SiO_2 (A), g-C_3N_4@SiO_2 (B) and P–C_3N_4 (C). TEM images of CoPdNPs (D), P–C_3N_4 (E) and P–C_3N_4-CoPdNPs (F). SEM images of FeMOFs (G) and FeMOFs-sCuO (H). EDX mapping images of P–C_3N_4-CoPdNPs (I).

literature (Fig. 2B, curve a) (Ma et al., 2013). Specific peaks of sCuO were found at 35.56°, 38.74°, 48.74°, 58.30°, and 68.13° (Fig. 2B, curve b), which corresponded to the planes of (−111), (111), (−202), (202) and (220), respectively. It can also be seen that the characteristic peak of the diffraction peak is relatively sharp, indicating that the crystal structure of the product is relatively complete. In addition, the XRD pattern of FeMOFs-sCuO composites also contained obvious characteristic peaks of FeMOFs and sCuO, which confirmed the successful synthesis of the composites.

The fourier transform infrared spectroscopy (FTIR) was used to explore the functional groups of the synthesized materials (Fig. S3). In the FeMOFs spectrum, the amino group and C═O bond in the organic linkers of the FeMOFs were the cause of the strong peak at 3470 cm^{-1} and 1658 cm^{-1}, respectively. The absorption peaks at 1390 $cm^{-1}$and 685 cm^{-1} were assigned to the C–O symmetric vibrations, and bending vibration inside and outside the plane of –COO group in FeMOFs, respectively. At 520 cm^{-1}, O–Fe–O bending vibrations in the FeMOFs were seen (Zangoa et al., 2020). As can be seen from the spectrum of sCuO, O–H stretching vibration of hydroxyl groups caused the infrared absorption peak at 3430 cm^{-1}. These hydroxy groups can form hydrogen bonds between molecules. It was worth noting that absorption signals appear at 718 cm^{-1}, 580 cm^{-1} and 493 cm^{-1}were caused by the stretching vibration of Cu–O (Meher and Rao, 2013). The FeMOFs-sCuO spectrum contained the characteristic absorption peaks of both FeMOFs and sCuO, which confirmed the successful synthesis of FeMOFs-sCuO.

By obtaining the Barrett-Joy-ner-Halenda pore size distributions and nitrogen adsorption-desorption isotherms of these g-C_3N_4 samples, the textural characteristics of these materials were further studied (Fig. 2D). The specific surface areas of g-C_3N_4 and P–C_3N_4 were found to be 248.52 and 339.04 m^2 g^{-1}. Additionally, the porosity within the nanoscale sheets of g-C_3N_4 is reflected in its 2–5 nm pore size dispersion. Compared with g-C_3N_4, P–C_3N_4 has a higher distribution at 10–25 nm, which was attributed to the formation of more holes after etched, while layer-stacked pores are responsible for the distribution appeared at 30–50 nm.

3.2. ECL mechanism

Herein, the enhancing and quenching strategies of ECL signal were illustrated by rigorous experiments. Fig. 3A showed the ECL strength of different luminescent material in PBS with $K_2S_2O_8$. The bulk g-C_3N_4 exhibited a low and unstable ECL signal, which was related to the block stacked structure of the original g-C_3N_4. The prepared P–C_3N_4 exhibited an evident ECL emission intensity, because the specific surface area of P–C_3N_4 was increased by etching of SiO_2, and more ECL luminophores in the inner layers can be activated. After modification of CoPdNPs on P–C_3N_4, a higher and more stable ECL signal was realized. However, as shown in Fig. S4, the ECL responses of both P–C_3N_4 (line a) and P–C_3N_4-CoPdNPs (line b) in PBS without $K_2S_2O_8$ were weak. Based on the above

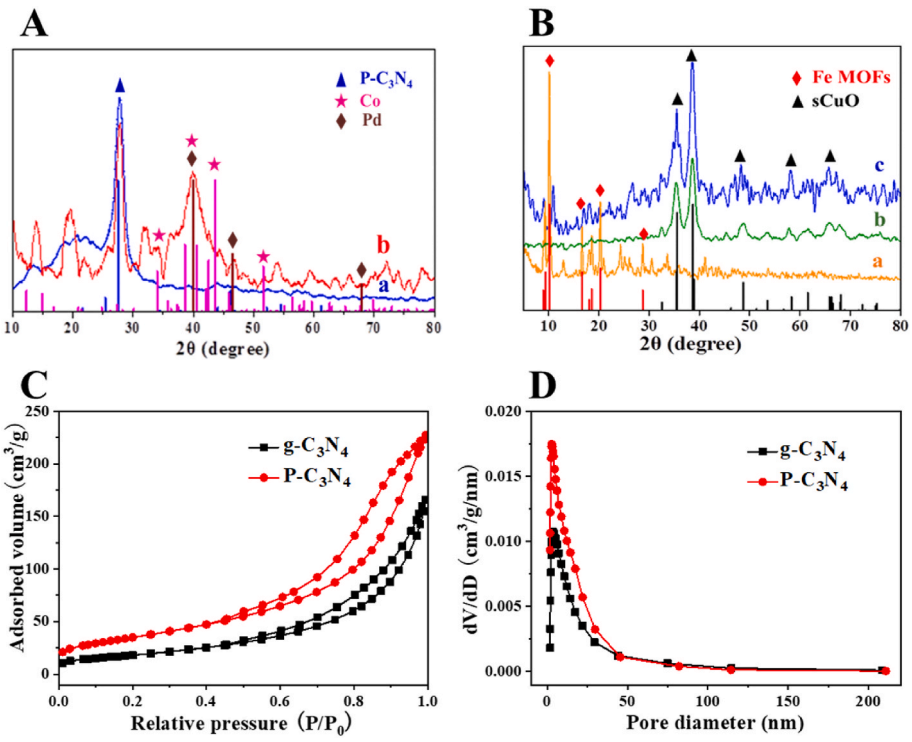

Fig. 2. (A) XRD of P–C_3N_4 (a) and P–C_3N_4-CoPdNPs (b). The standard XRD spectra of C_3N_4 (JCPDS 87–1526), Co (JCPDS 70–2633) and Pd (JCPDS 88–2335) were provided for comparison. (B) XRD of FeMOFs (a), sCuO (b) and FeMOFs-sCuO (c). The standard XRD spectra of Fe (JCPDS 72–0101), and CuO (JCPDS 89–5897) were provided for comparison. (C) N_2 adsorption/desorption isotherms of g-C_3N_4 and P–C_3N_4 and (D) the corresponding pore size distribution curves.

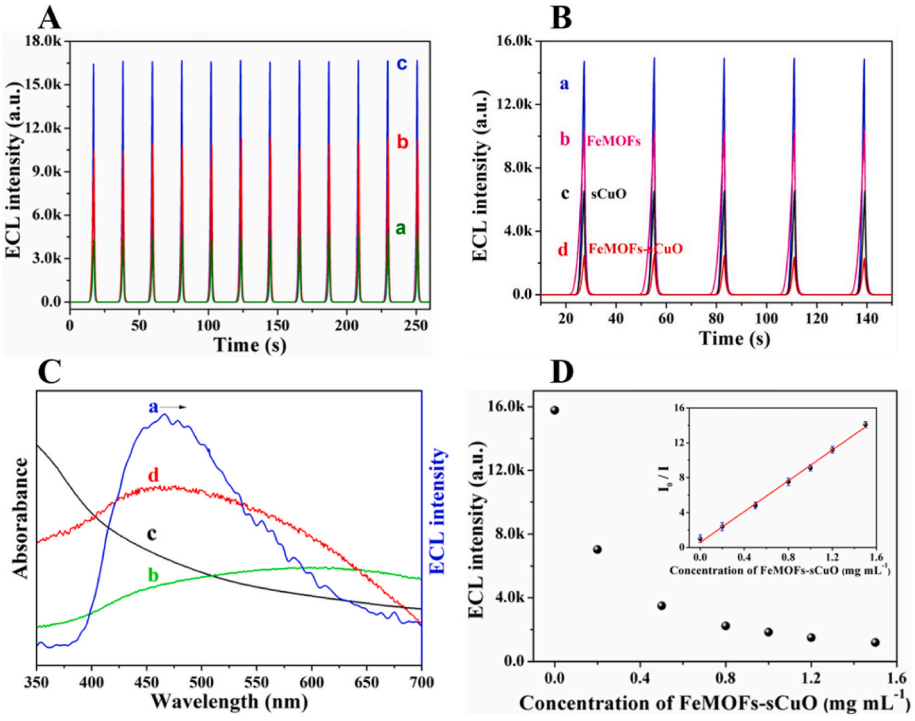

Fig. 3. (A) ECL intensity of g-C_3N_4 (a), P–C_3N_4 (b) and P–C_3N_4-CoPdNPs (c) in PBS with $K_2S_2O_8$. (B) ECL intensity of P–C_3N_4-CoPdNPs/GCE (a), FeMOFs/P–C_3N_4-CoPdNPs/GCE (b), sCuO/P–C_3N_4-CoPdNPs/GCE (c), and FeMOFs-sCuO/P–C_3N_4-CoPdNPs/GCE (d). (C) The ECL emission spectra of P–C_3N_4 (a) and UV–vis absorption of FeMOFs (b), sCuO (c) and FeMOFs-sCuO (d). (D) ECL intensity of P–C_3N_4-CoPdNPs in the existing of 0, 0.2, 0.5, 0.8, 1, 1.2, and 1.5 mg mL^{-1} FeMOFs-sCuO; The internal graphic represents to linear relationship. Error bars = RSD (n = 5).

results, the CoPdNPs were estimated to act on $K_2S_2O_8$ rather than directly on P–C_3N_4. To further explore the impact of CoPdNPs in the P–C_3N_4/$K_2S_2O_8$ system, electrodes modified with different materials were evaluated by CV experiment under various situations. The peak current of P–C_3N_4-CoPdNPs depicted in Fig. S5A has no obvious increases compared with that of P–C_3N_4 tested in PBS without $K_2S_2O_8$, demonstrating that there is no direct interaction between CoPdNPs and P–C_3N_4. Nevertheless, when the solution used in CV experiment was replaced with PBS containing $K_2S_2O_8$, CV curve of P–C_3N_4 reveals an apparent cathodic peak current (Fig. S5B), which was resulted from the electrocatalysis of $K_2S_2O_8$. When CoPdNPs and P–C_3N_4 were bound together, the peak current of P–C_3N_4-CoPdNPs further increased,

demonstrating that CoPdNPs can accelerate the reduction of $K_2S_2O_8$. The aforementioned information suggested that CoPdNPs might play a role of coreaction accelerator that can significantly increase the ECL emission of P–C_3N_4/$K_2S_2O_8$ system through interacting with $K_2S_2O_8$ rather than P–C_3N_4.

According to the relevant literature, the possible ECL enhancement mechanism of ternary (P–C_3N_4/$S_2O_8^{2-}$/CoPd) system was discussed (Zhou et al., 2020). When the voltage of the working electrode was continuously excited from −1.5 to 0 V, the radical anion of P–$C_3N_4^{\bullet-}$ could be produced by reduction of the P–C_3N_4 (eq (1)). Meanwhile, with the assistance of CoPdNPs, $S_2O_8^{2-}$ was reduced to the output massive amounts of $SO_4^{\bullet-}$ (eq (2)). Then the reduction product P–$C_3N_4^{\bullet-}$ and $SO_4^{\bullet-}$ interacted to form P–C_3N_4* (eq (3)). Eventually, the unstable P–C_3N_4* returned to the ground state, and intense emission and light were released (eq (4)).

$$p - C_3N_4 + e^- \rightarrow P - C_3N_4^{\bullet-} \quad (1)$$

$$S_2O_8^{2-} + e^- + \xrightarrow{\text{CoPd}} SO_4^{2-} + SO_4^{\bullet-} \quad (2)$$

$$P - C_3^{N_4^{\bullet-}}N_4^{\bullet-} + SO_4^{\bullet-} \rightarrow P - C_3N_4^* + SO_4^{2-} \quad (3)$$

$$P - C_3N_4^* \rightarrow P - C_3N_4 + h\nu \quad (4)$$

The quenching effects of FeMOFs-sCuO were also investigated (Fig. 3B), the emission of P–C_3N_4-CoPdNPs can be effectively extinguished by FeMOFs and sCuO, respectively. When the sCuO was combined with FeMOFs, FeMOFs-sCuO had a stronger quenching effect than that of FeMOFs or sCuO respectively. Therefore, FeMOFs-sCuO can be applied as a double quencher for P–C_3N_4 ECL emission. More experiments have been conducted to explore the quenching mechanism. As can be seen from the UV–Vis absorption spectrum of Fig. 3C, FeMOFs and sCuO have obvious and broad absorption peaks in the range of 400–650 nm and 300–550 nm, respectively. When the FeMOFs and sCuO were combined together, the UV–Vis absorption of FeMOFs-sCuO further broadened, which helped to increase the effective overlap between the UV–vis spectrum of FeMOFs-sCuO and the ECL emission spectrum of P–C_3N_4, thus enabling the ECL-RET process from P–C_3N_4-CoPdNPs (energy donor) to FeMOFs-sCuO (energy receptor). To get further insight into the quenching ability of FeMOFs-sCuO, the fluorescence spectra of P–C_3N_4 and its mixtures were recorded and the results were presented in Fig. S6. The fluorescence spectrum of P–C_3N_4 exhibited maximum emission at 434 nm and the excitation wavelength was at 380 nm (curve a). Obviously, the fluorescence emission intensity at 434 nm experienced a continuous decline after mixing with FeMOFs, sCuO and FeMOFs-sCuO (curve b, c and d), indicating that FeMOFs-sCuO was able to inhibit the fluorescence emission of P–C_3N_4.

To learn more about how well the FeMOFs-sCuO quencher works, the ECL quenching behavior towards P–C_3N_4-CoPdNPs was explored by using a range of contents of FeMOFs-sCuO in PBS buffer solution including 80 mM $K_2S_2O_8$. It can be seen from Fig. 3D, along with the concentration increase of FeMOFs-sCuO, the ECL signal decreased step by step. The corresponding linear relationship of I_0/I versus the concentrations of FeMOFs-sCuO was shown in the inside of Fig. 3D in the range from 0.0 to 1.5 g L^{-1} ($R^2 = 0.998$). In this step, I and I_0 were on behalf of ECL intensity with FeMOFs-sCuO and without, respectively. After fitting analysis and calculation, 8.744×10^6 g $^{-1}$ was obtained as the value of quenching constant (K_{sv}), which was evaluated according to the Stern-Volmer equation: $I_0/I = 1 + k_q\tau_0[Q] = 1 + K_{sv}[Q]$ (Xue et al., 2019). The excellent quenching effect of FeMOFs-sCuO was confirmed by all of the above results.

3.3. Optimization of the experimental conditions

Because the substrate, pH, quencher and co-reactant had a significant influence on the property of the manufactured biosensor, these conditions were explored in detail. Fig. S7A showed the impact of the P–C_3N_4-CoPdNPs substrate. When the P–C_3N_4-CoPdNPs concentration was less than 2.0 mg mL^{-1}, the ECL response intensity was in direct proportion to the concentration of P–C_3N_4-CoPdNPs. As the concentration of P–C_3N_4-CoPdNPs continues to increase, the signal intensity showed a slight downward trend. As a result, 2.0 mg mL^{-1} was defined as the best P–C_3N_4-CoPdNPs concentration. As shown in Fig. S7B, the ECL response showed a rising tendency when the pH value changed from 5.5 to 7.4. When the pH value increased from 7.4 to 8.5, the ECL intensity exhibited a slight decline phenomenon. Therefore, the most qualified pH value was chosen to be 7.4. Fig. S7C confirmed that the ECL strength of the system was closely related to the concentration of $K_2S_2O_8$, with a positive proportional increase relationship. ECL signal reached its maximum value at the concentration of 80 mM and did not increase significantly when the concentration continued to exceed 80 mM. Therefore, 80 mM $K_2S_2O_8$ could fully satisfy the test consumption and was determined as the best co-reaction agent condition. Fig. S7D showed the influence of the change of quenching agent concentration. When the concentration of FeMOFs-sCuO was 1.5 mg mL^{-1}, the quenching effect was the best. So the optimal quencher concentration was 1.5 mg mL^{-1}.

3.4. Characterization of the immunosensor

The characteristics between ECL strength and voltage of different modified electrodes in the construction process was used to verify that the biosensor was successfully manufactured, and the consequences were displayed in Fig. 4A. The undecorated working electrode generated a weak ECL signal (curve a). The P–C_3N_4-CoPdNPs was excited at the working electrode and showed a significant ECL response (curve b). The ECL intensity in the system was gradually reduced after modifying Ab_1, dripping BSA and casting NSE onto the working electrode, successively (curve d, curve e and curve g), because the electron transfer was hindered by Ab_1, BSA, and NSE. As can be seen, the ECL intensity of GCE/P–C_3N_4-CoPdNPs/FeMOFs-sCuO (curve c) was close to that of GCE/P–C_3N_4-CoPdNPs (curve b), the ECL intensity of GCE/P–C_3N_4-CoPdNPs/Ab_1/BSA/FeMOFs-sCuO (curve f) was also close to that of GCE/P–C_3N_4-CoPdNPs/Ab_1/BSA (curve e). This is due to that FeMOFs-sCuO has no obvious interaction between P–C_3N_4-CoPdNPs or BSA, most of the FeMOFs-sCuO was washed away when the as-prepared electrode was softly rinsed with PBS buffer solution. When FeMOFs-sCuO-Ab_2 was continued to be added, the electrode suffered a significant ECL inhibition (curve h), indicating the high quenching efficiency of the quenching label FeMOFs-sCuO-Ab_2. The results showed that the biosensor was successfully manufactured by layered modification.

Electrochemical impedance spectroscopy (EIS) tests on different modified electrodes also provided further support for the immunosensor's construction process (Fig. 4B). The Nyquist plots can be simulated based on the inset equivalent circuit. ZSimpWin software was used for simulation analysis of the proposed sensor strategy, and the specific simulation values were shown in Table S1. The intercept of the semicircle at Z' axis in the high-frequency region represents the solution resistance of the electrolyte nearby electrode (R_s), the semi-circle in the high to medium-frequency region is associated with the charge transfer and redox reaction resistance (R_{et}) and double layer capacitance (C_d), and the straight line in the low frequency is related to the Warburg impedance (Z_w) due to diffusion. As can be seen from Table S1, the values of R_s, C_d, and Z_w changed very little. The main concern here is the change in R_{et}, which reflected the diffusion retardation of the electroactive marker at the electrode interface. Fig. 4B showed that the EIS curve of bare GCE was almost a straight line (curve a), because the electron transfer process was almost free. Curve b was a small semicircle on the EIS spectrum, indicating that the impedance value of the electrode modified by P–C_3N_4-CoPdNPs was low, which confirmed that CoPdNPs gave excellent conductivity to the substrate material. The Ab_1, BSA and NSE (curve c to curve e) were continuously modified on the

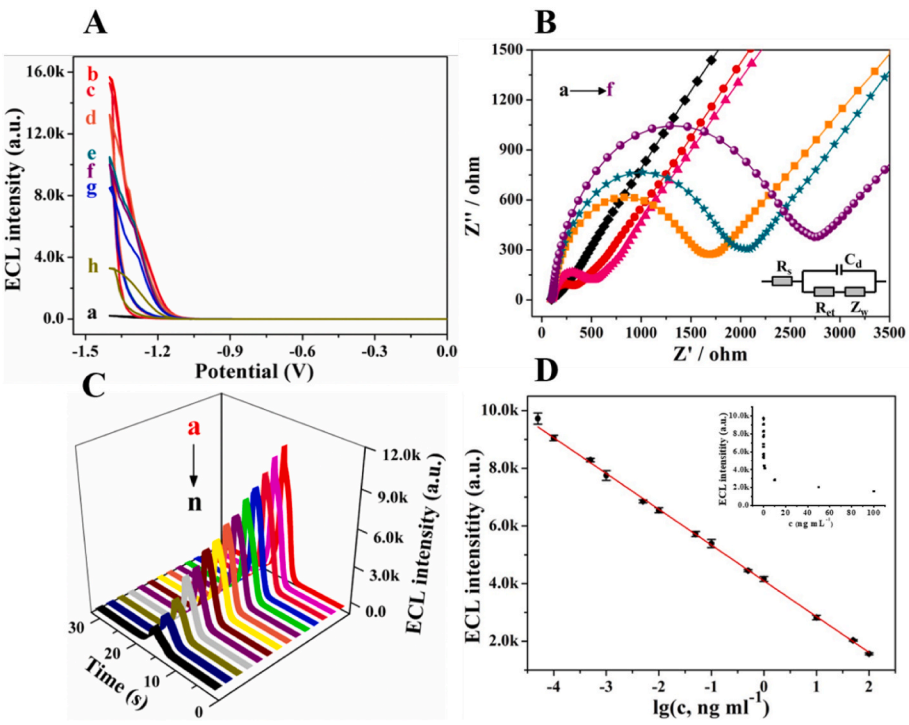

Fig. 4. (A) The ECL intensity-potential curves of GCE (a), GCE/P–C_3N_4-CoPdNPs (b), GCE/P–C_3N_4-CoPdNPs/FeMOFs-sCuO (c), GCE/P–C_3N_4-CoPdNPs/Ab_1 (d), GCE/P–C_3N_4-CoPdNPs/Ab_1/BSA (e), GCE/P–C_3N_4-CoPdNPs/Ab_1/BSA/FeMOFs-sCuO (f), GCE/P–C_3N_4-CoPdNPs/Ab_1/BSA/NSE (g), GCE/P–C_3N_4-CoPdNPs/Ab_1/BSA/NSE/FeMOFs-sCuO-Ab_2 (h) in PBS (pH = 7.4) containing 80 mM $K_2S_2O_8$ and 0.1 M KCl. (B) The corresponding EIS in 2.5 mM $Fe(CN)_6^{3-/4-}$ and 0.1 M KNO_3. (C) ECL response of the immunosensor to different concentrations of NSE, from a to n: 0, 0.0000500, 0.000100, 0.000500, 0.00100, 0.00500, 0.0100, 0.0500, 0.100, 0.500, 1.00, 10.0, 50.0 and 100 ng mL^{-1}. (D) The calibration curve of the immunosensor for different concentrations of NSE. Error bars = RSD (n = 5).

electrode surface, and the impedance values progressively increased in EIS spectrum, because these substances hindered electron transfer as nonelectroactive substances. Finally, when the working electrode was modified with FeMOFs-sCuO-Ab_2, the R_{et} value reached the maximum (curve f), confirming that the immunoreactions occurred between NSE antigen and Ab_2 biological conjugate. The double quenching biosensor was successfully constructed, based on the aforementioned results.

3.5. Analytical ability of the biosensor

With the most appropriate measuring parameters, the ECL strength of NSE at different concentrations was measured to appraise the sensing property of the immunosensor. As depicted in Fig. 4C, in the NSE concentration range of 0.0000500–100 ng mL^{-1}, the ECL intensity of the quench-type sensor was gradually reduced by biological immune recognition. According to the test results, the calibration curve of the sensor was obtained by fitting analysis (Fig. 4D), and the linear regression equation I_{ECL} = 4096.51–1241.28 × lg c with a correlation coefficient of 0.997 was reliable. To determine the limit of detection (LOD) and limit of quantification (LOQ) of the fabricated sensor, the mean values from the blank measurements (ECL response of the immunosensor to 0 ng mL^{-1} of NSE, five replicates) plus 3 and 10 times the standard deviation (SD), respectively (Kim et al., 2018). According to the calculated results of the above linear regression equation, the LOD, and LOQ of the prepared ECL sensor for NSE analysis are 20.4 fg mL^{-1} and 7.99 fg mL^{-1}, respectively, with the relative standard deviation (RSD) of 1.68%. The linear detection range was 0.0000500–100 ng mL^{-1}. Compared with other detection schemes (Table S2), the lower LOD with a broad detection range in this work might originate from that P–C_3N_4-CoPdNPs has significant ECL emission property and FeMOFs-sCuO has prominent quenching performance.

3.6. Application performance of the immunosensor

Protein markers similar to the target antigen were usually used to evaluate the specificity of immunosensors as interfering substances. Carcinoembryonic antigen (CEA), β-Amyloid (Aβ), prostate specific antigen (PSA), procalcitonin (PCT) and alpha fetoprotein (AFP) were common antigens in our choice of interfering substances. As shown in Fig. 5A, when the detection object contained only one of the aforementioned interferents, the ECL responses did not significantly differ from the experimental blank. Additionally, when 1 ng mL^{-1} of NSE or a combination of NSE and the aforementioned interferences were added to the immunosensor, the ECL responses were almost the same. The above results indicated an acceptable selectivity specificity of this ECL immunosensor.

Precision intra and inter assays under the same experimental condition was used to study the repeatability of the biosensor for NSE. As shown in Fig. 5B, the RSD values of the intra- (cure a) and inter-assay (cure b) experiment were 1.92% and 1.36%, respectively, indicating a good reproducibility of this biosensor.

The immunosensor's practical applicability also depends on stable operation. As shown in Fig. 5C, the electrode was scanned for 12 cycles under consecutively potential after being modified with 0.1 ng mL^{-1} of NSE, which showed nice stability with the RSD of 1.32%. The long-term storage stability of the proposed immunosensor was also evaluated (Fig. S8). After storage at 4 °C for 15 days, the ECL intensity of the immunosensor has no dramatic changes, indicating a satisfactory storage stability. The outcomes showed that the immunosensor that was built has dependable stability.

3.7. Sample analysis

Recovery analysis was performed in human serum samples using standard addition method to further assess the viability of the ECL biosensor for NSE detection. The acquired serum's NSE concentration was analyzed to be 0.450 ng mL^{-1} by using immunosensor manufactured here (denoted as detected concentration). The recovery analysis results displayed in Table S3 was 96.0–103%, which confirmed that the proposed immunosensor with superb performance can perform clinical samples detection well. In addition, an enzyme-linked immunosorbent assay (ELISA) kit was used as a comparison method. The F test was used to determine the precision of the designed ECL immunosensor and ELISA Kit. As shown in Table S4, the calculated F value is lower than the 6.39

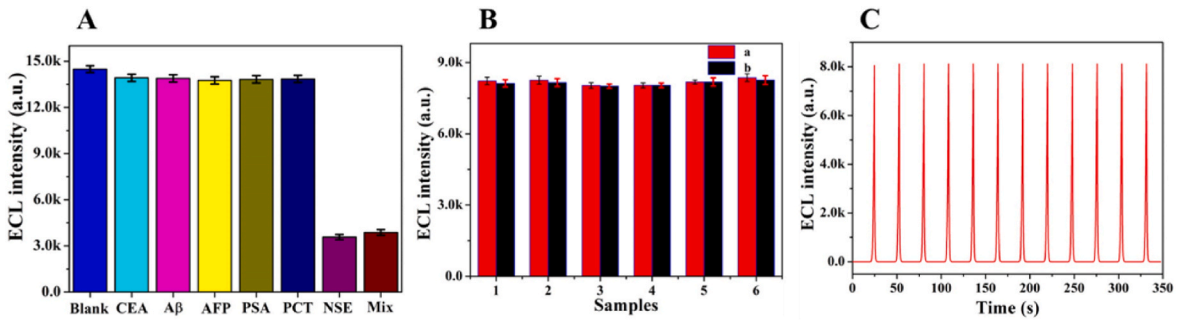

Fig. 5. (A) The ECL behavior of the immunosensors to recognize 10 ng mL^{-1} CEA, Aβ, AFP, PSA, PCT and 1 ng mL^{-1} NSE. (B) Intra- (a) and inter-assay (b) carried out to estimate the repeatability of the biosensor for NSE, (C) The stability of the ECL immunosensor for 12 cycles. Error bars = RSD (n = 5).

(at 95% confidence limits), which indicated no significant difference between the two methods (Wu et al., 2022). The *t*-test was also used to assess the accuracy of the method through comparing the mean values (Y. Li et al., 2020). The t value is less than 2.78 (P = 0.95, α = 0.05, f = 4). The above results revealed that the developed ECL sensing platform displayed potential feasibility for NSE analysis in serum samples.

4. Conclusion

In brief, a novel quenching ECL immunosensor was firstly developed based on the ECL-RET interaction between P–C_3N_4-CoPdNPs donor and FeMOFs-sCuO recipient to achieve sensitive determination of NSE. Herein, CoPdNPs were firstly loaded onto P–C_3N_4 to improve the ECL performance of P–C_3N_4, generating a high-efficiency luminescent material P–C_3N_4-CoPdNPs. Meanwhile, small-sized CuO nanoparticles and FeMOFs were first coupled to achieve a double quenching effect, which significantly increased the sensitivity of the biosensor. In the end, the detection limit of the prepared ECL sensor for NSE analysis was downgrade to 20.4 fg mL^{-1} (S/N = 3), with a broad detection range of 0.0000500–100 ng mL^{-1}. In addition, the immunosensor has excellent specificity, repeatability and stability. Therefore, this new sensing method showed potential application prospect in clinical diagnosis.

CRediT authorship contribution statement

Lihua Hu: conceived and designed the experiments, analyzed the data and revised the manuscript. **Tengfei Shi:** Writing – original draft, conceived and designed the experiments, performed the experiments, analyzed the data and wrote the original draft of the manuscript. **Jiye Chen:** contributed substantially to revisions. **Qianqian Cui:** contributed substantially to revisions. **Hao Yu:** contributed substantially to revisions. **Dan Wu:** contributed substantially to revisions. **Hongmin Ma:** contributed substantially to revisions. **Qin Wei:** contributed substantially to revisions. **Huangxian Ju:** contributed substantially to revisions. All the authors discussed the results and commented on the manuscript, Yuyang Li conceived and designed the experiments.

Declaration of competing interest

The authors declare that they have no known competing financial interests or personal relationships that could have appeared to influence the work reported in this paper.

Data availability

No data was used for the research described in the article.

Acknowledgements

This study was supported by the National Natural Science Foundation of China (Nos. 21607055, 21675063, 21775054, 21505051, 21575050, 21777056), National Key Scientific Instrument and Equipment Development Project of China (No.21627809).

Appendix A. Supplementary data

Supplementary data to this article can be found online at https://doi.org/10.1016/j.bios.2023.115132.

References

Amani, J., Maleki, M., Khoshroo, A., Sobhani-Nasab, A., Rahimi-Nasrabadi, M., 2018. Anal. Biochem. 548, 53–59.
Cao, J.T., Fu, X.L., Zhao, L.Z., Ma, S.H., Liu, Y.M., 2020. Sensor. Actuator. B Chem. 311, 127926.
Chen, W., Chen, J., Feng, Y.B., Hong, L., Chen, Q.Y., Wu, L.F., Lin, X.H., Xia, X.H., 2012. Analyst 137, 1706–1712.
Daglar, H., Gulbalkan, H.C., Avci, G., Aksu, G.O., Altundal, O.F., Altintas, C., Erucar, I., Keskin, S., 2021. Angew. Chem., Int. Ed. 60, 7828–7837.
Dalkiran, B., Brett, C.M.A., 2022. Microchem. J. 179, 107531.
Din, M.I., Khalid, R., Hussain, Z., 2022. J. Mol. Liq. 358, 119181.
Erbaycu, A.E., Gunduz, A., Batum, O., Ucar, Z.Z., Tuksavul, F., Guclu, S.Z., 2010. Arch. Bronconeumol. 46, 364–369.
Feng, D., Tan, X., Wu, Y., Ai, C., Luo, Y., Chen, Q., Han, H., 2019. Biosens. Bioelectron. 129, 100–106.
Fu, X., Yang, Y., Wang, N., Chen, S., 2017. Sensor. Actuator. B Chem. 250, 584–590.
Hu, M., Wang, Y., Yang, J., Sun, Y., Xing, G., Deng, R., Hu, X., Zhang, G., 2019. Biosens. Bioelectron. 142, 111554.
Kim, H., Sohn, A., Yeo, I., Yu, S.J., Yoon, J.H., Kim, Y., 2018. Clin. Chem. 64, 1230–1238.
Li, X.J., Du, Y., Wang, H., Ma, H.M., Wu, D., Ren, X., Wei, Q., Xu, J.J., 2020. Anal. Chem. 92, 12693–12699.
Li, Y., Gu, M., Zhang, X., Fan, J., Lv, K., Carabineiro, S.A.C., Dong, F., 2020. Mater. Today 41, 270–303.
Liu, J.L., Jiang, J., Zhang, J.Q., Chai, Y.Q., Xiao, Q., Yuan, R., 2020. Biosens. Bioelectron. 152, 112006.
Luan, Q., Xiong, X., Gan, N., Cao, Y., Li, T., Wu, D., Dong, Y., Hu, F., 2018. Talanta 187, 27–34.
Ma, E., Wang, P., Yang, Q., Yu, H., Pei, F., Zheng, Y., Liu, Q., Dong, Y., Li, Y., 2020. ACS Biomater. Sci. Eng. 6, 1418–1427.
Ma, M., Bétard, A., Weber, I., Al-Hokbany, N.S., Fischer, R.A., Metzler-Nolte, N., 2013. Cryst. Growth Des. 13, 2286–2291.
Majdoub, M., Anfar, Z., Amedlous, A., 2020. ACS Nano 14, 12390–12469.
Meher, S.K., Rao, G.R., 2013. Nanoscale 5, 2089–2099.
Pan, Y., Su, H.Q., Zhou, E.L., Yin, H.Z., Shao, K.Z., Su, Z.M., 2019. Dalton Trans. 48, 3723–3729.
Rahbar, N., Salehnezhad, Z., Hatamie, A., Babapour, A., 2018. Microchim. Acta 185, 101.
Song, J.T., Chen, Z.X., Cai, X.B., Zhou, X., Zhan, G.L., Li, R.L., Wei, P.P., Yan, N., Xi, S.B., Loh, K.P., 2018. Adv. Mater. 34, 2204638.
Sun, C.Y., To, W.P., Hung, F.F., Wang, X.L., Su, Z.M., Che, C.M., 2018. Chem. Sci. 9, 2357–2364.
Tang, Y., Hu, X.P., Liu, Y.W., Chen, Y.R., Zhao, F.Q., Zeng, B.Z., 2022. Biosens. Bioelectron. 214, 114492.
Wang, S., Zhan, J., Chen, K., Ali, A., Zeng, L., Zhao, H., Hu, W., Zhu, L., Xu, X., 2020. ACS Sustain. Chem. Eng. 8, 8214–8222.
Wang, Y., Zhang, Y., Sha, H., Xiong, X., Jia, N., 2019. ACS Appl. Mater. Interfaces 11, 36299–36306.
Wang, Y., Zhang, Y., Yan, T., Fan, D., Du, B., Ma, H., Wei, Q., 2016. Biosens. Bioelectron. 80, 640–646.
Wang, Z., Huang, Y., Chen, M., Shi, X., Zhang, Y., Cao, J., Ho, W., Lee, S.C., 2019. ACS Appl. Mater. Interfaces 11, 10651–10662.
Wu, T.T., Du, Y., Dai, L., Li, J.S., Song, X.Z., Feng, J.H., Wang, X.Y., Wei, Q., Ju, H.X., 2022. Anal. Chem. 94, 10651–10658.

Xu, R.H., Liao, C.Z., Luo, Y., Xu, W.L., Li, K., Chen, J.X., Huang, Y.F., Chen, Y.C., Zhu, L., Yuan, W.B., 2015. Clin. Chim. Acta 440, 188–192.
Xuan, Z.H., Wu, Y.X., Liu, H.M., Li, L., Ye, J., Wang, S.X., 2021. Sensors 21, 6538.
Xue, J.W., Yang, L., Jia, Y., Zhang, Y., Wu, D., Ma, H.M., Hu, L.H., Wei, Q., Ju, H.X., 2019. Biosens. Bioelectron. 142, 111524.
Ye, Y., Liu, H., Li, Y., Zhuang, Q., Liu, P., Gu, J., 2019. Talanta 200, 472–479.
Zangoa, Z., Bakarb, N., Sambudic, N., Jumbria, K., Abdullaha, N.A., Kadird, E., Saad, B., 2020. J. Environ. Chem. Eng. 8, 103544.
Zhang, Y., Wang, F., Zhang, H., Wang, H., Liu, Y., 2019. Anal. Chem. 91, 12100–12107.
Zhang, Y.W., Liu, W.S., Chen, J.S., Niu, H.L., Mao, C.J., Jin, B.K., 2020. Sensor. Actuator. B Chem. 321, 128456.
Zhao, C., Jiang, Z., Mu, R., Li, Y., 2016. Talanta 159, 365–370.
Zhao, Y.X., Chen, Q.M., Zhang, C., Li, C.N., Jiang, Z.L., Liang, A.H., 2022. Biosensors 12, 920.
Zhou, X., Zhang, W., Wang, Z., Han, J., Xie, G., Chen, S., 2020. Biosens. Bioelectron. 148, 111795.
Zou, J.Y., Li, L., You, S.Y., Liu, Y.W., Cui, H.M., Cui, J.Z., Zhang, S.W., 2018. Dalton Trans. 47, 15694–15702.